Energy & Environmental Science

ROYAL SOCIETY OF CHEMISTRY

PAPER

View Article Online
View Journal

Cite this: DOI: 10.1039/d4ee02815e

Bicontinuous-phase electrolyte for a highly reversible Zn metal anode working at ultralow temperature†

Mi Xu,‡[a] Beinuo Zhang,‡[a] Yudong Sang,[a] Dan Luo,[a] Rui Gao,[b] Qianyi Ma,[b] Haozhen Dou*[ab] and Zhongwei Chen *[ab]

Received 27th June 2024,
Accepted 20th September 2024

DOI: 10.1039/d4ee02815e

rsc.li/ees

Hybrid electrolytes utilizing organic solvents as cosolvents or additives present tremendous promise for low-temperature aqueous zinc ion batteries (ZIBs). However, the nanostructure of hybrid electrolytes has been rarely investigated, leaving a knowledge gap between the atomistic solvation structure and macroscopic battery performance. Herein, the nanostructure of hybrid electrolytes was systematically studied, and a new concept of bicontinuous-phase electrolyte (BPE) is proposed. By carefully adjusting the volume ratio of H_2O and organic solvent, a BPE with a three-dimensional interpenetrating aqueous phase and organic phase is obtained, which delivers an optimal Zn^{2+} transfer number of 0.68 and fast desolvation kinetics. More importantly, the BPE possesses a well-balanced organic solvent-rich solvation sheath and anion-involved solvation sheath and generates a uniform *in situ* solid electrolyte interface with an organic-rich outer layer and inorganic-rich inner layer. The BPE affords ultralong cycling stability for about 4700 hours at −20 °C and boosts stability at an ultralow temperature of −60 °C, outperforming most low-temperature ZIBs. Equally intriguingly, the Zn anode exhibits record-breaking reversibility over 13 000 hours at room temperature. Impressively, Zn‖V_2O_5 batteries show an excellent capacity retention of 100% for over 1100 cycles at −60 °C and over 2000 cycles under high mass loading (14 mg cm^{-2}), lean electrolyte conditions (E/C ratio = 8.7 μL mA^{-1} h^{-1}), and limited Zn supply (N/P ratio = 2.55). This study provides an in-depth understanding of the nanostructures of hybrid electrolytes, which opens a universal avenue toward high-performance low-temperature batteries.

Broader context

The sustainable growth of large-scale renewable energy highly calls for efficient and temperature-adaptable energy storage technologies. Aqueous zinc ion batteries (ZIBs) have emerged as the leading candidates for large-scale energy storage owing to their high safety, low cost, and environmental friendliness. However, aqueous electrolytes tend to get frozen at subzero temperatures, which results in a dramatic drop in ion transport and sluggish interfacial dynamics. Currently, hybrid electrolytes can effectively improve the temperature adaptability of ZIBs, and their nanostructures play a decisive role in low-temperature performance. However, the nanostructure of hybrid electrolytes for ZIBs has been overlooked, leaving a knowledge gap between the atomistic solvation structure and macroscopical battery performance. In this work, a bicontinuous-phase electrolyte (BPE) with a three-dimensional interpenetrating aqueous phase and organic phase is obtained, which delivers the optimal Zn^{2+} transfer number of 0.68 and fast desolvation kinetics. Moreover, the BPE possesses a well-balanced organic solvent-rich solvation sheath and anion-involved solvation sheath and generates a uniform *in situ* solid electrolyte interface. As a result, the BPE endows ZIBs with an ultralow operating temperature of −60 °C and ultralong cycling life at subzero temperatures. This work provides a novel perspective for designing high-performance electrolytes for low-temperature ZIBs *via* nanostructure optimization.

Introduction

Rechargeable aqueous zinc ion batteries (ZIBs) have emerged as the promising alternative battery technology for grid-scale energy storage applications in the post-lithium era[1–3] owing to their cost effectiveness, intrinsic safety, facile manufacturing, eco-friendliness and high theoretical capacity.[4,5] Decreasing battery operating temperature to low temperature is

[a] State Key Laboratory of Catalysis, Power Battery & System Research Center, Dalian Institute of Chemical Physics, Chinese Academy of Sciences, Dalian, 110623, China. E-mail: haozhen@dicp.ac.cn, zwchen@dicp.ac.cn
[b] Department of Chemical Engineering, University of Waterloo, Waterloo, ON N2L 3G1, Canada

† Electronic supplementary information (ESI) available. See DOI: https://doi.org/10.1039/d4ee02815e

‡ M. X. and B. Z. contributed equally to this work.

imperative for renewable energy utilization in winter, frigid regions[6–8] or other scenarios such as polar expedition and interplanetary exploration.[9–11] Despite their high safety, aqueous electrolytes inevitably induce ubiquitous dendrite growth and water-related side reactions, such as corrosion and the hydrogen evolution reaction (HER), thus resulting in the poor coulombic efficiency and extremely limited cycling lifespan of ZIBs.[12–16] More particularly, under subzero temperatures, aqueous electrolytes tend to freeze with a sharp increase in viscosity, which results in reduced ionic conductivity, poor wettability toward the electrode, and sluggish interfacial dynamics, thereby deteriorating battery performance.[17,18] Thus far, three main types of electrolytes have been developed for low-temperature ZIBs, including high concentrated ''water in salt'' electrolytes, deep eutectic solvents and hybrid electrolytes.[19–31] Among them, hybrid electrolytes utilizing organic solvents as cosolvents or additives are the most fascinating owing to their structural designability, low cost and feasibility of practical applications.[32–36]

Benefiting from the abundant hydrogen-bond acceptor–donor sites and structural diversity of organic solvents,[37–41] hybrid electrolytes deliver low-temperature applicability because of hydrogen-bond reconstruction and can maintain the non-flammability and high safety of aqueous electrolytes by rationally selecting the boiling point of the cosolvent or additive.[42] Besides, the organic solvent in hybrid electrolytes can effectively optimize the Zn^{2+} solvation structure and/or preferential adsorption on the Zn anode, which can regulate side reactions and contribute to controllable Zn^{2+} deposition to inhibit dendrite growth. Currently, protic and aprotic organic solvents, such as methanol, 2-propanol, ethylene glycol, tetrahydrofuran, *N*,*N*-dimethylformamide, *N*,*N*-dimethyl acetamide, propylene carbonate, and dimethyl sulfoxide (DMSO), have been demonstrated for low-temperature ZIBs.[43] Despite great efforts, the battery performance of hybrid electrolytes under subzero temperatures is not satisfactory (Table S1, ESI†). The cycling life is always restricted to 1000 hours and the operating temperature is generally higher than −40 °C due to the absence of system optimization of the electrolyte structure, where the volume fraction of organic solvents is arbitrarily fixed in the range of 10–40%.[44–46] Most importantly, it is well acknowledged that the ions and molecule self-assembly under electrostatic interaction, hydrogen-bond interaction and dipole-ion interactions contribute to the formation of the distinct electrolyte nanostructure, such as molecular clusters/aggregates, nanodomains, or percolating network, which determines the ion transport path, ion diffusion flux, and transference number. Moreover, the electrolyte nanostructure effectively alters the properties of the electrode/electrolyte interface to mitigate side reactions and dendrite growth, which are closely related to the overall electrochemical performance of the battery, such as the cycle life, rate capability, and low-temperature performance, and are widely recognized in lithium batteries. However, the nanostructure of hybrid electrolytes has been overlooked and rarely investigated for ZIBs, leaving a knowledge gap between the atomistic solvation structure and macroscopic battery performance.

Herein, by selecting DMSO as a paradigm, for the first time, we investigate the nanostructure of hybrid electrolytes with a large range of H_2O/DMSO volume ratio from 2 : 1 to 1 : 2 and elucidate the relationship of ''Zn^{2+} solvation shell-electrolyte nanostructure-macroscopic battery permeance'', which establishes selection criteria for the organic solvent/H_2O ratio to obtain the best low-temperature performance. By carefully adjusting the volume ratio of H_2O and organic solvent, a bicontinuous-phase electrolyte (BPE) with a three-dimensional interpenetrating aqueous phase and organic phase is obtained, which delivers the highest Zn^{2+} transfer number and fast desolvation kinetics, thus affording long-lasting ZIBs capable of ultralow-temperature (−60 °C) operation. DMSO is a Lewis base with a high electron pair donor and a high donor number (29.8, Table S2, ESI†), confining the H_2O within the BPE networks *via* hydrogen-bond interactions, which significantly restrains water activity to suppress side reactions and lowers the freezing point of BPE (< −100 °C). Importantly, experiments together with theoretical calculations suggest that BPE obtains a well-balanced DMSO-rich solvation sheath and anion-involved solvation sheath and induces the *in situ* formation of a uniform SEI consisting of an organic-rich outer layer and an inorganic-rich inner layer. Compared with the previous results with an improved cycling life of around 1000 hours, Zn‖Zn symmetric cells with BPE deliver an order of magnitude high cycling life of over 13 000 hours at 0.5 mA h cm^{-2} and over 640 hours at high areal capacity of 10 mA h cm^{-2}. Remarkably, BPE endows the Zn anode with a long cycling life of nearly 5000 hours at −20 °C and 1350 hours at an ultralow temperature of −60 °C, which outperforms the lowest-temperature ZIBs based on electrolyte engineering. Moreover, the Zn‖V_2O_5 batteries show an excellent capacity retention of 100% for over 1100 cycles at −60 °C and over 2000 cycles under practical conditions (high mass-loading of 14 mg cm^{-2}, lean electrolyte of 8.7 μL mA^{-1} h^{-1}, and low N/P ratio of 2.55), and BPE is demonstrated in multi-layer pouch cells.

Results and discussion

Design of a bicontinuous-phase electrolyte

DMSO is a highly polar aprotic solvent, and its high donor number suggests that it can manipulate hydrogen-bond networks among water molecules to decrease the freezing point of electrolytes and generate strong interaction with electrophilic metal cations to tailor the solvation structure. Therefore, DMSO has been utilized to broaden the temperature range of hydrogel electrolytes[47] and decrease the freezing point of aqueous electrolytes for rechargeable alkali-ion batteries.[48] Although DMSO has been reported as an additive (volume fraction <20%) to tailor $ZnSO_4$ aqueous electrolyte to regulate the solvation structure or $ZnCl_2$ aqueous electrolyte to promote the interface stability in ZIBs,[49,50] how DMSO works at low temperatures (< −40 °C) ZIBs has not been verified, especially on the effect of electrolyte nanostructure on low-temperature batteries. A series of hybrid electrolytes with H_2O/DMSO volume ratios of 2 : 1,

1 : 1 and 1 : 2 can be obtained by dissolving 2 m $Zn(CF_3SO_3)_2$ into an H_2O–DMSO mixed solvent, which are denoted as HD21, HD11, and HD12, respectively (Fig. S1, ESI†). Analogously, the baseline electrolyte with a 2 m $Zn(CF_3SO_3)_2$ aqueous electrolyte is denoted as a ZFE (HD10). Notably, hybrid electrolytes do not sacrifice the high safety of aqueous electrolytes due to the high boiling point of DMSO (Fig. S2, ESI†) and witness the broader electrochemical stability window relative to ZFE (Fig. S3, ESI†). Moreover, a significantly low freezing point below −100 °C is achieved for HD11 owing to the reconstruction of strong hydrogen-bond (HB) interactions between H_2O and DMSO (Fig. S4, ESI†), as further recognized by the frost-resistant experiment (Fig. S5, ESI†), thus allowing for low-temperature working of ZIBs. More importantly, HD11 maintains a high ion conductivity of 1.5 mS cm^{-1} at −60 °C, while ion conductivity of ZFE drastically decreases to 0 mS cm^{-1} at −60 °C (Fig. S6, ESI†).

The nanostructure of hybrid electrolytes is identified by molecular dynamics (MD) simulation and wide-angle X-ray scattering (WAXS). As visualized by the highlighted MD snapshots, the nanostructure of hybrid electrolytes delivers the transformation from "DMSO in H_2O" to "H_2O in DMSO" with the volume ratio varying from 2 : 1 to 1 : 2. The aggregation of H_2O molecules proceeds from highly hydrogen-bonded aggregation to a scattering state, which resides in cavities between DMSO and $CF_3SO_3^-$ species (Fig. S7, ESI†). As further evidenced by the isosurface images for the ion and molecule of electrolytes from the MD simulation (Fig. 1a–c and Fig. S8, ESI†), the DMSO phase and H_2O phase are discreetly distributed in HD21 and HD12, respectively. Bicontinuous sponge-like nanostructures with the continuous aqueous phase and continuous organic solvent phase are ubiquitous in HD11. As shown in Fig. 1d, the lower q value of scattering bands for hybrid electrolytes indicates the enlarged size of the ion–molecule coordination cluster. The WAXS patterns and images of HD11 show the narrowest scattering bands with enhanced intensity (Fig. 1d and e), which suggests the well-defined bicontinuous-phase nanostructure with uniformly distributed coordination clusters.

More interestingly, the HD11 obtains the maximal Zn^{2+} transference number (0.68) (Fig. 1f and Fig. S9, ESI†) due to the percolation networks, indicating that the bicontinuous nanostructure can shorten the Zn^{2+} transfer route and guide the Zn^{2+} fast migration, which is key to support good battery performance at low temperature. As further highlighted by the electrochemical impedance spectroscopy (EIS) of symmetric Zn‖Zn cells at various temperatures (Fig. 1g and Fig. S10, ESI†), HD11 exhibits much lower charge transfer resistance (R_{ct}) than that of ZFE, especially at low temperatures. Subsequently, the Arrhenius activation energy (E_a) is calculated, which represents the desolvation barrier of the hydrated Zn^{2+} on the electrode/electrolyte interface. The resultant E_a with HD11 (39.35 kJ mol^{-1}) is much lower when compared to that of ZFE

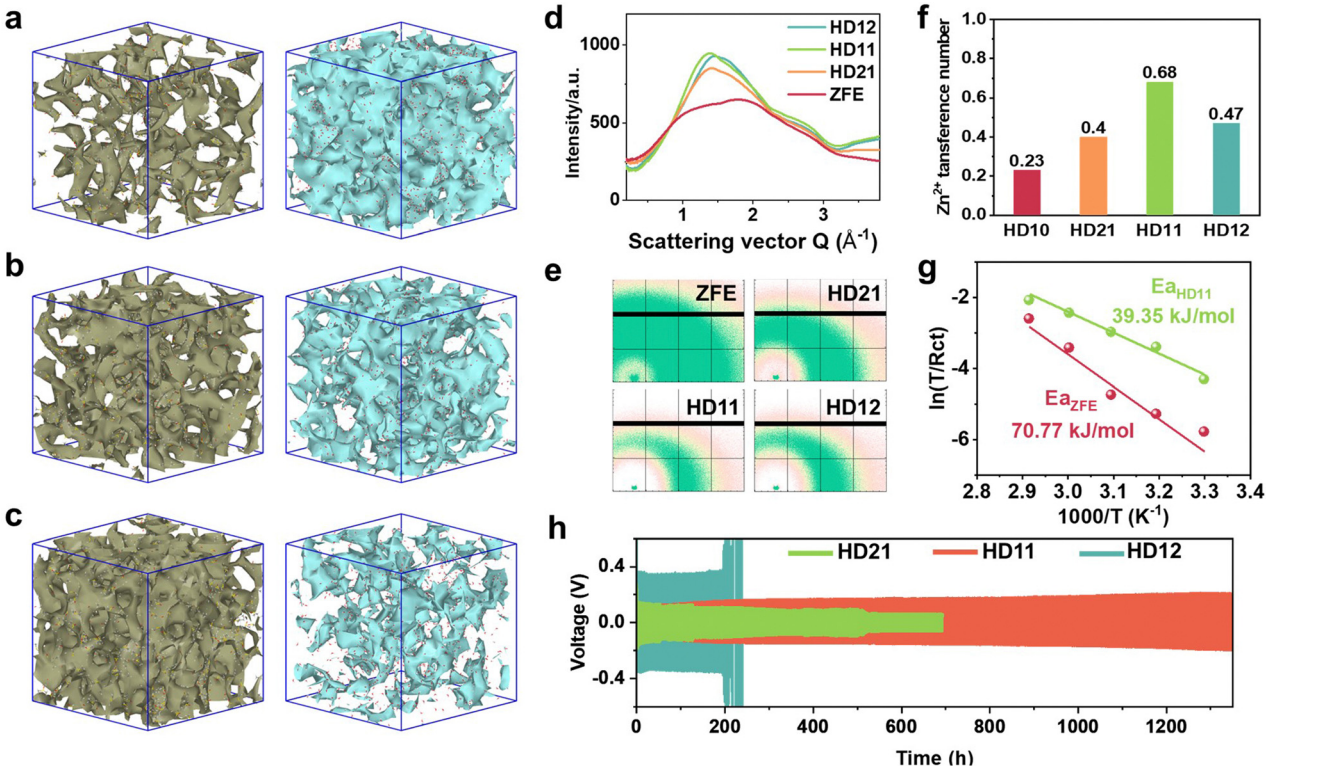

Fig. 1 Bicontinuous-phase electrolyte design and nanostructure study. (a)–(c) Isosurface images of DMSO molecules (left) and H_2O molecules (right) in HD21 (a), HD11 (b) and HD12 (c) electrolytes. (d) Wide-angle X-ray scattering (WAXS) patterns of different electrolytes. (e) Two-dimensional WAXS image; (f) Zn^{2+} transference number. (g) Arrhenius curves and corresponding activation energies. (h) Cycling performance of the Zn‖Zn asymmetric cell at −60 °C.

(70.77 kJ mol^{-1}), verifying the accelerated desolvation process of hydrated Zn^{2+} due to the bicontinuous-phase nanostructure. Remarkably, HD11 affords a Zn‖Zn symmetric cell with the best low-temperature performance, which exhibits a cycling life of near 1400 hours at an ultralow temperature of −60 °C benefiting from high Zn^{2+} transfer number and fast kinetics (Fig. 1h). Based on the above findings, the concept of bicontinuous-phase electrolyte (BPE) is proposed to highlight the structure and property advance of the bicontinuous phase hybrid electrolytes, and BPE (HD11) is utilized for the following investigation.

Intermolecular interactions and ingredients of the solvation structure

The intermolecular interactions and solvation structures of BPE are investigated by characterization experiments and theoretical calculations. As demonstrated by density functional theory (DFT) calculations (Fig. 2a and Fig. S11, ESI†), both $CF_3SO_3^-$ and DMSO molecules can feasibly destroy the HB networks between H_2O molecules and form stronger new HB with H_2O molecules, which is conducive to suppressing HER. Moreover, the binding energy of Zn^{2+}–DMSO (−195.49 kcal mol^{-1}) is larger than that of Zn^{2+}–H_2O (−107.88 kcal mol^{-1}) due to the

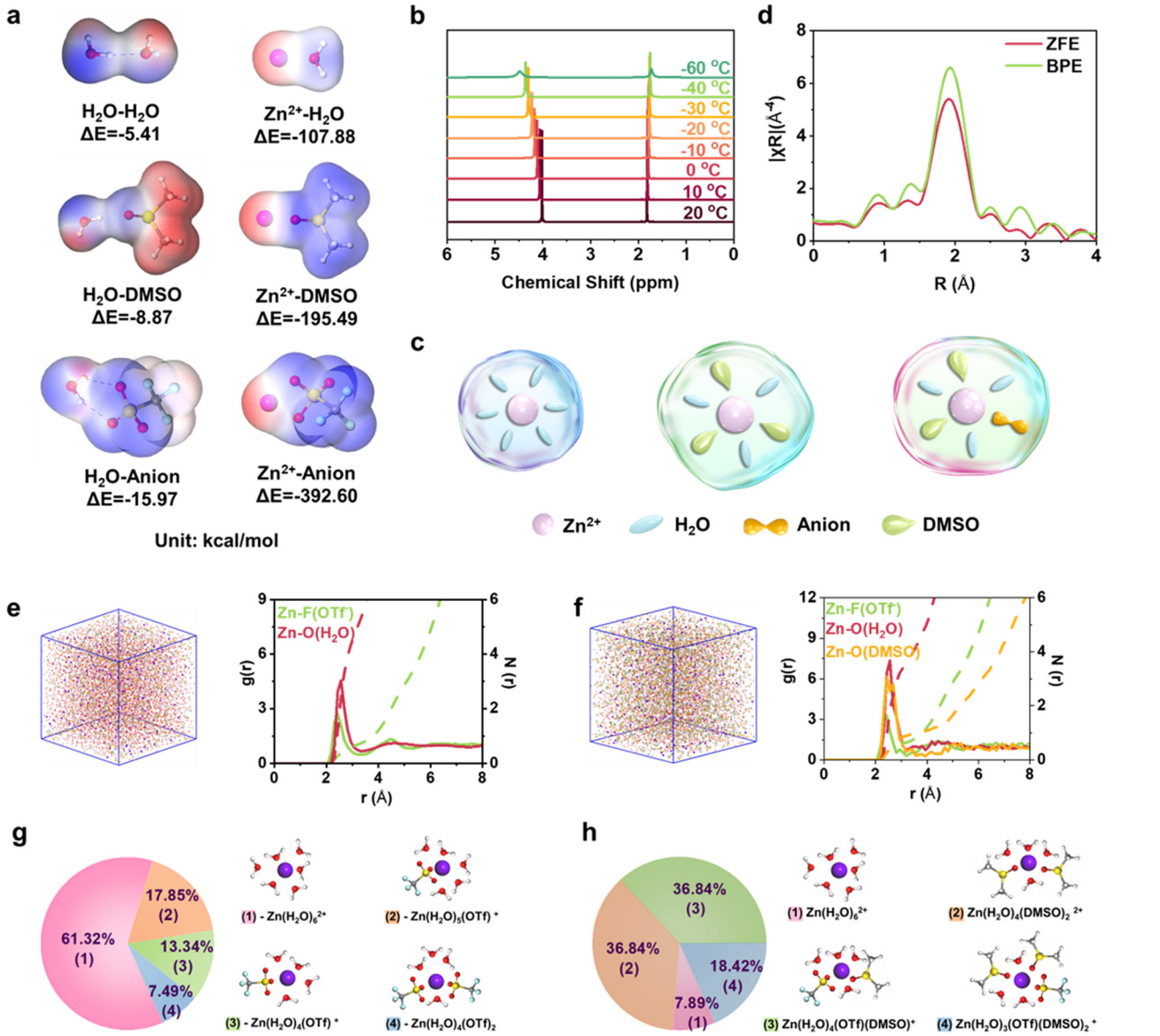

Fig. 2 Solvation structure and intermolecular interactions. (a) Electrostatic potential mapping and binding energy between any two constituents of the BPE. (b) ^{1}HNMR spectra of the BPE at different temperatures. (c) Schematics of the Zn^{2+} solvation sheath for the ZFE (left) and BPE (middle and right). (d) Fourier transformation of Zn K-edge extended X-ray absorption fine structure (EXAFS) spectra of the ZFE and BPE. (e) Molecular dynamics (MD) simulation of the ZFE, and the corresponding radial distribution functions and coordination number (CN) of Zn^{2+}–H_2O and Zn^{2+}–Otf. (f) Molecular dynamics (MD) simulation of the BPE, and the corresponding radial distribution functions and coordination number (CN) of Zn^{2+}–H_2O, Zn^{2+}–OTf, and Zn^{2+}–DMSO. (g) and (h) Distributions of possible inner solvation sheath ingredients of the ZFE and BPE from MD simulation.

rich electron density of DMSO, which suggests that DMSO can effectively tailor Zn^{2+} solvation sheath. Subsequently, nuclear magnetic resonance (NMR) spectroscopy, attenuated total reflectance Fourier transform infrared (ATR-FTIR) spectroscopy and Raman spectroscopy are performed to analyze the intermolecular interplay of BPE. In the ^{1}H NMR spectra (Fig. S12, ESI†), the chemical shift of H_2O gradually moves downfield with the increase in DMSO content, which indicates the formation of stable and stronger HB networks between H_2O and DMSO. Similarly, ^{19}F NMR spectra undergo downfield shifts along with the increase in DMSO content, indicating the enhanced interaction between $CF_3SO_3^-$ anion and Zn^{2+} (Fig. S13, ESI†). More importantly, ^{1}H NMR spectra of BPE at variable temperatures from 25 °C to −60 °C reveal the increased peak width but decreased intensity of OH and CH_3 groups (Fig. 2b and Fig. S14, ESI†), which convincingly proves the restricted molecule motility and enhanced molecule association. Low temperature induces stronger HB interactions, as recognized by the downfield shift of the OH group and the upfield shift of the CH_3 group. ATR-FTIR spectroscopy further highlights the newly formed HB interactions between DMSO and H_2O and enhanced interactions between Zn^{2+} and $CF_3SO_3^-$ anion (Fig. S15, ESI†). Moreover, Raman spectroscopy is performed to shed light on the intermolecular interplay (Fig. S16, ESI†). The stretching vibration bands of CH_3 and C–S of DMSO move to higher wavenumbers, which suggests strong interactions between Zn^{2+} and DMSO, thus remodeling the Zn^{2+} solvation structure. Meanwhile, the SO_3 stretching vibration band of the $CF_3SO_3^-$ anion exhibits blue shifts, which suggests that the free anion reduces, and the aggregated ion cluster increases, implying that $CF_3SO_3^-$ anions enter into the Zn^{2+} solvation sheath. The Zn^{2+} solvation sheath of BPE is investigated by X-ray absorption spectroscopy and molecular dynamics (MD) simulations, which indicate that the BPE has two main solvation sheaths: DMSO-rich solvation sheath and anion-involved solvation sheath (Fig. 2c). Zn X-ray absorption near-edge structure (XANES) spectra demonstrate that Zn K edge position of BPE shifts to lower energy with reference to ZFE, which implies that the effective positive charge around Zn^{2+} decreases upon the introduction of DMSO due to more electronic donation from DMSO and anion to Zn^{2+} (Fig. 2d and Fig. S17, ESI†). The radial distance corresponding to the Zn–O bond increases slightly in BPE, verifying the loose solvation structure owing to the high steric effect of the anion and DMSO, which is consistent with the results of WAXS. The wavelet transform of EXAFS indicates the unchanged Zn–O coordination for both ZFE and BPE. MD simulations are performed to gain insight into the solvation structure of BPE, where the radial distribution function (RDF, $g(r)$) and corresponding coordination number (CN) are obtained (Fig. 2e, f and Fig. S18, S19, ESI†). In the BPE, the RDF of Zn^{2+}–DMSO exhibits a sharp peak around 2.3 Å, indicating that DMSO participates in the Zn^{2+} solvation sheath. As indicated by the CN, the Zn^{2+} solvation sheath of ZFE contains 5.7 H_2O, while the Zn^{2+} solvation sheath of BPE is composed of 3.8 H_2O, 1.2 DMSO, and 1 $CF_3SO_3^-$. The systematic analysis of the solvation structure indicates that the CN of Zn^{2+}–DMSO gradually increases from 0.7 to 1.6 and the CN of Zn^{2+}–$CF_3SO_3^-$ increases from 0.9 to 1.3 with H_2O/DMSO volume ratio changing from 2 : 1 to 1 : 2. Therefore, the increase in DMSO encourages more anion and DMSO to enter into Zn^{2+} solvation sheath, and BPE possesses the anion-involved and DMSO-rich solvation sheath.

More specifically, the main Zn^{2+} solvation sheaths and their distribution in ZFE and BPE are performed, and HD21 and HD12 are also included for comparison (Fig. 2g, h and Fig. S20, ESI†). In the ZFE, the typical solvation sheath of $Zn(H_2O)_6^{2+}$ is dominant with a high proportion of 61.32%, which rapidly decreases to 7.89% for BPE. The primary and secondary solvation sheaths of BPE are $[Zn(H_2O)_4(DMSO)_2]^{2+}$ and $[Zn(H_2O)_4(CF_3SO_3^-)(DMSO)]^+$, whose proportions are the same (36.84%). Therefore, BPE possesses a well-balanced DMSO-rich solvation sheath and an anion-involved solvation sheath. Compared with HD21 and HD12, the proportion of the anion-involved solvation sheath or DMSO-rich solvation sheath in BPE is nearly twice higher than that of HD21 and is close to that of HD12 due to the well-defined nanostructure with a bicontinuous phase structure. Therefore, BPE can effectively suppress hydrogen evolution side reactions and essentially improve the electrochemical stability of the Zn anode *via* anion-derived interface chemistry when compared with HD21. Meanwhile, BPE obtains faster mass transfer kinetics compared with HD21, especially considering the highest Zn^{2+} transfer number. Moreover, as quantified by DFT calculations (Fig. S21 and S22, ESI†), the higher Gibbs free energy means a high tendency to form DMSO-rich solvation sheath and anion-involved solvation sheath in thermodynamics, which can reduce the water activity to suppress HER, guide Zn^{2+} deposition to inhibit dendrite growth, and induce anion- and DMSO-dominant interface chemistry.

Structure and formation mechanism of the SEI

The interface chemistry of Zn anode in BPE and its correlation with solvation structure are analysed by time-of-flight secondary-ion mass spectrometry (TOF-SIMS), in-depth X-ray photoelectron spectroscopy (XPS) and transmission electron microscopy (TEM). TOF-SIMS is applied to investigate the three-dimensional elemental distribution of the Zn anode (Fig. 3a and Fig. S23, ESI†). In BPE, O, S, F and C signals are mainly distributed on the Zn anode surface, and Zn element distribution exhibits a flat and uniform top surface, which suggests the formation of thin and dense SEI. The C content of the Zn anode cycled in BPE is significantly higher than that in ZFE, confirming the participation of DMSO decomposition in the formation of the SEI due to the primary DMSO-rich solvation sheath. Moreover, light–dark alternating element distribution confirms the ''Mosaic model'' SEI. In contrast, the Zn anode cycled in ZFE exhibits a deep and gradient C, O, S and F distribution, and the O element is completely dispersed in the entire sputtering box, which suggests unremitting side reactions due to the absence of the SEI layer. The chemical compositions of the SEI layer are investigated by in-depth XPS (Fig. 3b and Fig. S24, S25, ESI†). In the F1s spectra,

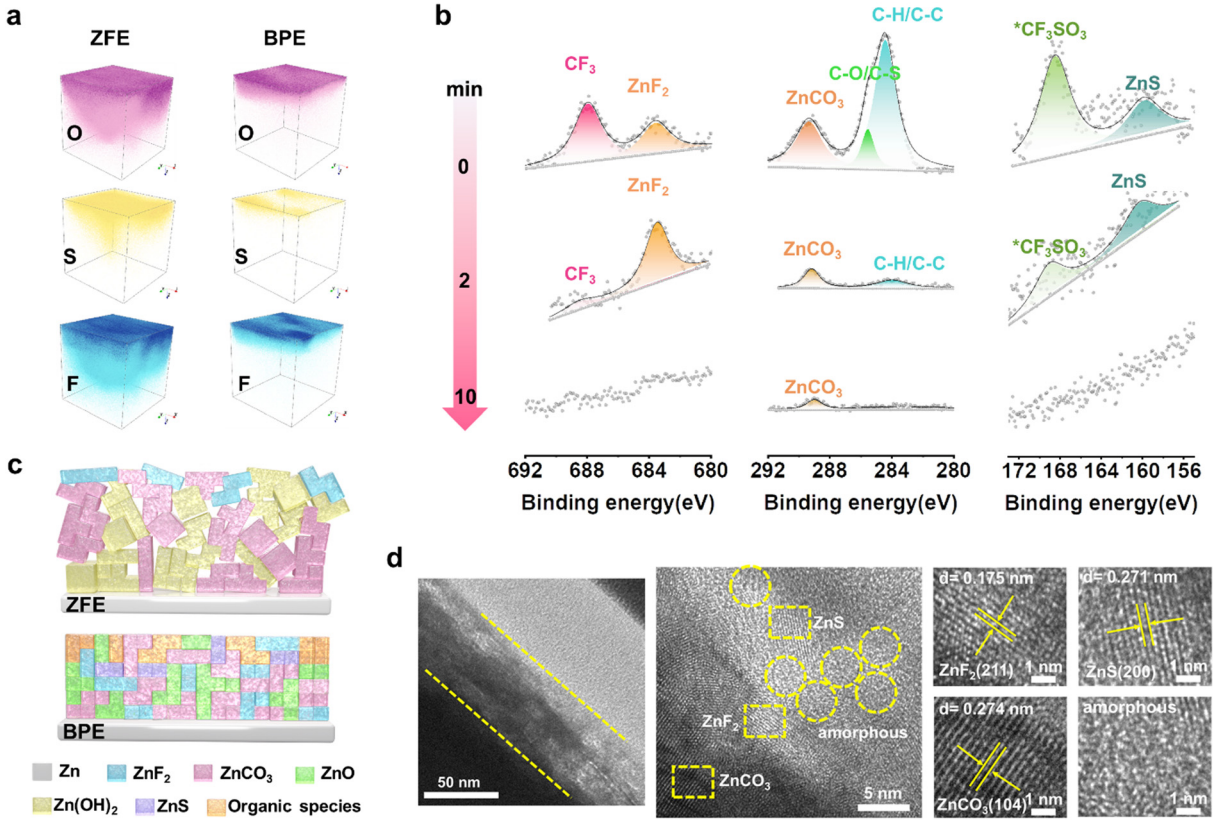

Fig. 3 Identification of SEI chemistry and structure. (a) Time-of-flight secondary-ion mass spectrometry (TOF-SIMS) characterization for element spatial distribution within the SEI layer. (b) XPS spectra for F1s, C1s and S2p elements of Zn anode cycled in BPE at different etching times. (c) Schematic diagrams for Mosaic SEI. (d) HR-TEM images of organic and inorganic components within the SEI layer of BPE.

both organic fluorine (CF_3) at 688.4 eV and inorganic fluorine (ZnF_2) at 684.6 eV are observed on the Zn anode, and organic fluorine is mainly distributed on the surface of SEI layer, which indicates that the $CF_3SO_3^-$ anions participate in the formation of the SEI layer *via* electrochemical decomposition. With the increase in Ar^+ etching time to 2 min, the ZnF_2 content significantly increases compared with that on the surface, suggesting the organic-rich upper layer and inorganic-rich sublayer of SEI. In the C1s XPS spectra, the peaks at 289.7, 285.8 and 284.8 eV are attributed to $ZnCO_3$, C–O/C–S and C–H/C–C, respectively, and the C–H/C–C component possesses the highest content on the surface. The C–H/C–C component arises from the decomposition of DMSO or $CF_3SO_3^-$ anion, the C–O/C–S component is mainly derived from DMSO decomposition, and $ZnCO_3$ results from either $CF_3SO_3^-$ anion decomposition or dissolved CO_2 in BPE. In-depth component analysis indicates that organic carbon species enrich in the upper layer of SEI and inorganic carbon species are abundant in the sublayer of SEI. The S2p XPS spectra confirm the existence of $*CF_3SO_3$ (168.3 eV) and ZnS (162.1 eV), which verifies the decomposition of $CF_3SO_3^-$ anions, which is in accordance with the F1s spectra.

Remarkably, as evidenced by in-depth XPS, low-temperature SEI exhibits similar chemical components with room-temperature SEI except for a few alterations of the content and distribution of certain components (Fig. S26, ESI†). For example, C1s and O1s XPS spectra show an organic-rich upper layer and an inorganic-rich sublayer, and F1s XPS spectra confirm the existence of inorganic ZnF_2 and organic CF_3 in the low-temperature SEI layer, but both the upper layer and sublayer of SEI contain a higher ZnF_2 component. Low-temperature SEI shows similar carbon components, but the C–O/C–S species becomes the dominant component, which is attributed to the different effects of temperature on interfacial reaction kinetics. Moreover, the Zn metal content of the low-temperature SEI is much higher than that of the room-temperature SEI at the same etching time, which suggests a thinner SEI layer at low temperatures, which is similar to the thinner low-temperature SEI of lithium metal batteries. Therefore, *in situ* generation of a ''Mosaic model'' SEI with an organic-rich upper layer and inorganic-rich sublayer is achieved in BPE at both room and low temperatures (Fig. 3c). Therefore, the primary DMSO-rich solvation sheath and secondary anion-involved solvation sheath of BPE contribute to the preferential decomposition of DMSO and $CF_3SO_3^-$ anion, thus forming a dense and compact SEI layer. The structure of the SEI layer formed in BPE is also observed by TEM. A clear SEI layer with a thickness of 50 nm is observed with mosaic component distribution, which comprises amorphous organic components and highly crystalline inorganic components. As highlighted by

high-resolution TEM, the inorganic components are $ZnCO_3$, ZnS and ZnF_2, which are actually consistent with the XPS results (Fig. 3d).

Electrochemical characterization of the Zn anode and morphological evolution

The favorable electrolyte structure and compact SEI layer effectively boost the Zn anode reversibility, which has been proven by the Zn‖Zn symmetric cell, Zn‖Cu and Zn‖Ti asymmetric cells. Zn‖Zn cell using BPE can stably perform over 13 000 hours at a current density of 0.5 mA cm^{-2} and an areal capacity of 0.5 mA h cm^{-2} (Fig. 4a). The small polarization voltage suggests fast Zn plating/stripping kinetics, revealing that BPE enables highly reversible Zn chemistry. On the contrary, the Zn anode with ZFE exhibits an extremely short cycling life of 64 hours (Fig. S27, ESI†). In detail, voltage profiles highlight the quite stable performance in BPE, but large voltage fluctuation and sudden short circuits occur in ZFE. More importantly, BPE affords the longest cycling life among all the designed hybrid electrolytes due to the bicontinuous-

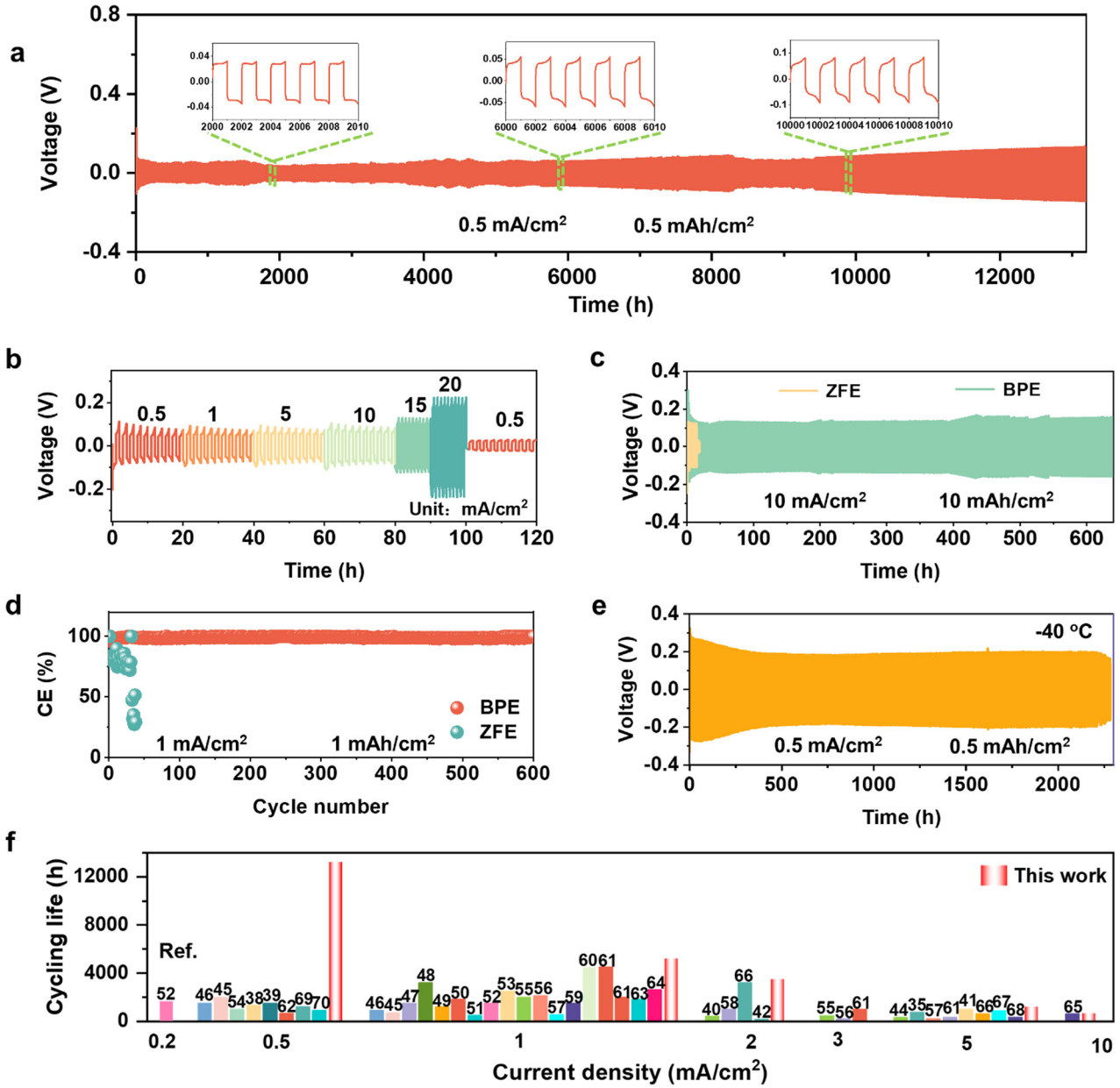

Fig. 4 Plating/stripping behaviors of the Zn anode at both room and low temperatures. (a) Galvanostatic cycling performance of Zn‖Zn symmetric cells at 0.5 mA cm^{-2} and 0.5 mA h cm^{-2} under 25 °C. (b) Rate performance of Zn‖Zn symmetric cell at different current densities. (c) Galvanostatic cycling performance of Zn‖Zn symmetric cells at high DOD (85.4%, 10 mA cm^{-2} and 10 mA h cm^{-2}). (d) CE of Zn‖Ti asymmetric cell at 1 mA cm^{-2} and 1 mA h cm^{-2} under 25 °C. (e) Galvanostatic cycling performance of Zn‖Zn symmetric cells at 0.5 mA cm^{-2} and 0.5 mA h cm^{-2} under −40 °C. (f) Comparison of cycling performance of Zn‖Zn symmetric cells in this work with other reported hybrid electrolytes at room temperature.

phase nanostructure (Fig. S28, ESI†). Zn‖Zn symmetric cell shows the stable striping/plating voltage profiles as current densities change from 0.5 mA cm^{-2} to 20 mA cm^{-2}, demonstrating the excellent rate performance (Fig. 4b and Fig. S29, ESI†). A significantly extended lifespan is achieved even at high current densities with 1-hour striping and 1-hour plating, over 5600 hours, 3500 hours, and 1200 hours at current densities of 1 mA cm^{-2}, 2 mA cm^{-2}, and 5 mA cm^{-2}, respectively (Fig. S30, ESI†). Moreover, the symmetric cell delivers a cycling life of over 640 hours at a high depth of discharge (DOD) of 85.4% before short-circuit triggered by dendrite growth (Fig. 4c). The coulombic efficiency (CE) of BPE is determined in asymmetrical Zn‖Ti cells at a current density of 1 mA cm^{-2} and capacity of 1 mA h cm^{-2}. The Zn‖Ti cell with ZFE displays a fluctuant and a low CE of around 79.23%, which can only maintain stable cycling for less than 70 hours (Fig. 4d and Fig. S31, ESI†). Contrastingly, high cycling stability for more than 1200 hours has been achieved in BPE, accompanied by a high and stable CE of 99.85%, indicating that high reversibility of the Zn anode was enabled by the BPE. The high CE of BPE is further evidenced in the Zn‖Cu cell (Fig. S32, ESI†). Excellent long-term cycling performance is also achieved with BPE at low temperatures. The long-term cycling stability for over 2300 hours and 4500 hours is achieved under −40 °C and −20 °C (Fig. 4e and Fig. S33, ESI†). As highlighted in Fig. 4f, the ultra-long cycling life of the Zn‖Zn symmetric cell surpasses most of the reported hybrid electrolytes in the literature, strongly confirming the superiority of BPE for highly reversible Zn anode.[35,38–42,44–46,49–72]

Zn anode morphology is investigated by multiscale characterizations. SEM images indicate that many small-sized protuberances appear on the Zn anodes cycled in ZFE after the 1st cycle. Zn anode surface shows a highly porous/mossy structure, which is haphazardly overgrown with plate-like Zn dendrites after 30 cycles. With the continuous Zn plating/stripping for 100 cycles, large-sized Zn dendrites are formed, which easily penetrate the glass fiber to cause battery failure (Fig. 5a and Fig. S34, ESI†). In sharp contrast, the Zn anode cycled in BPE presents a uniform and smooth surface even after 100 cycles. The cross-section morphology of the Zn anode after 30 cycles is studied by focused ion beam scanning electron microscopy (FIB-SEM). The Zn anode in ZFE reveals a 2 μm-thick cycled

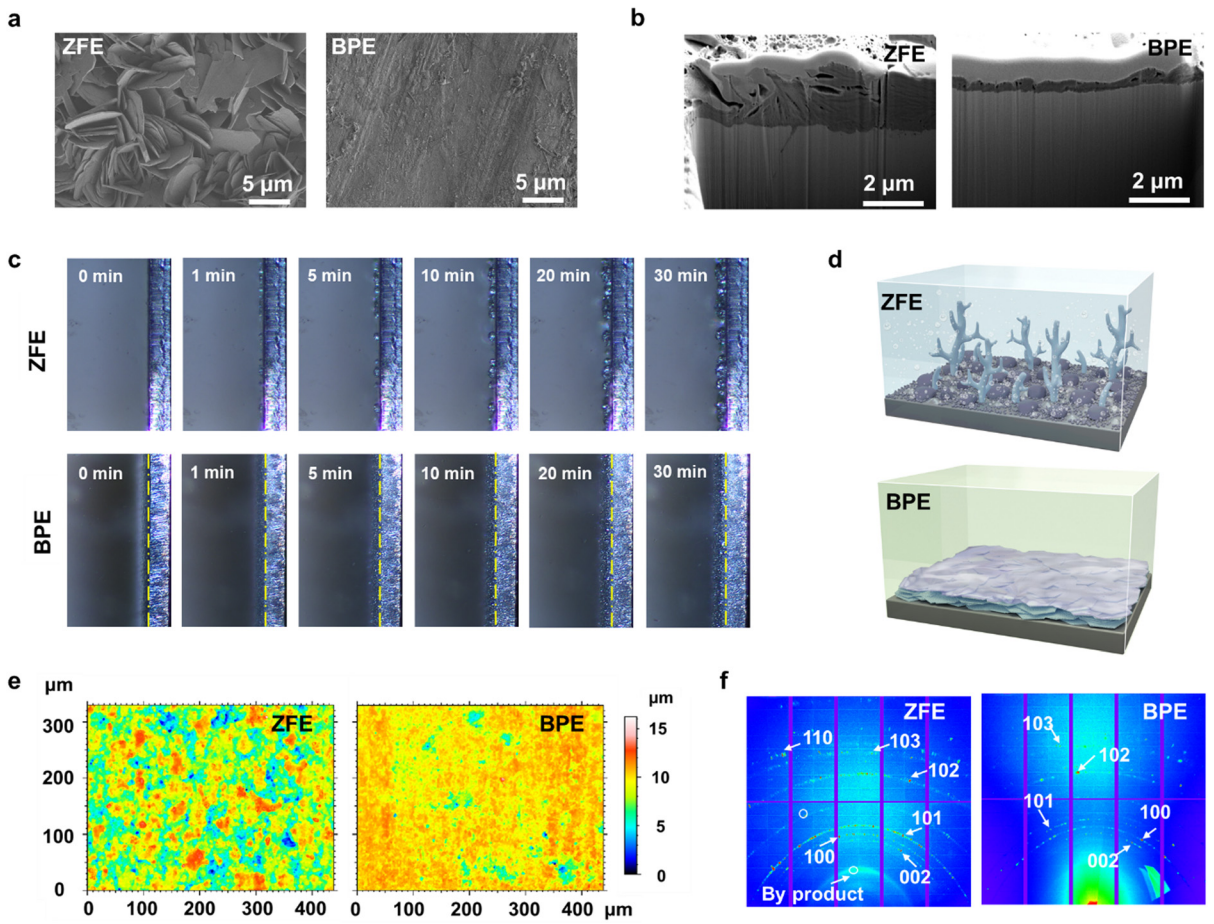

Fig. 5 Multiscale characterization for electrodeposition microstructure of the Zn anode in the ZFE and BPE. (a) SEM images of the Zn anode after 30 cycles. (b) FIB-SEM images of the Zn anode after 30 cycles. (c) *In situ* optical microscope images of Zn plating at a current density of 5 mA cm^{-2}. (d) Schematics of the Zn anode interface structure cycled in the ZFE and BPE. (e) 3D LCSM images of the Zn anode after 30 cycles. (f) 2D-GIXRD images of the Zn anode after 30 cycles.

layer with random metal branching and porous packing, while dense packing of Zn anode is observed in BPE with a cycled layer thickness of around 300 nm (Fig. 5b and Fig. S35, ESI†). Even at long-term cycling times (1000–5000 hours) under high current density (1–5 mA cm^{-2}), Zn anodes exhibit different textures but retain the uniform morphology without Zn dendrite (Fig. S36, ESI†). Moreover, Zn anodes at −20 °C and −60 °C present the uniform and dendrite-free morphology (Fig. S37, ESI†). Remarkably, only some small-sized Zn plates can be observed after 4000-hour cycling (Fig. S38, ESI†), indicating that the BPE can effectively relieve Zn dendrite at low temperatures.

Further, Zn nucleation and deposition behavior are studied by combining *ex situ* and *in situ* characterizations. As indicated by contact angle measurement, BPE exhibits better wettability towards metal anodes than ZFE, which promotes the facile Zn^{2+} transport at the electrode/electrolyte interface (Fig. S39, ESI†). Chronoamperometry (CA) is conducted to characterize the Zn^{2+} diffusion on the Zn anode. In the ZFE, the current response is continuously increasing, indicating a continuous 2D diffusion process, which is caused by the increase in the effective electrode area due to dendrite growth (Fig. S40, ESI†). Conversely, for zinc anode cycled in BPE, the current response shows an inappreciable change beyond the initial 100 s, suggesting the hindered 2D surface diffusion to favour even and uniform Zn deposition. Moreover, BPE is capable of homogeneous Zn nucleation. As recognized by cyclic voltammograms, Zn nucleation overpotential increases gradually, which is attributed to reduced electron tunneling. Higher overpotential corresponds to a stronger driving force for nucleation, which leads to a smaller nucleus radius and finer Zn grains (Fig. S41, ESI†).

The Zn^{2+} plating process is visualized by *in situ* optical microscopy at a current density of 5 mA cm^{-2}. In ZFE, scattered dendrites (bright spots) emerge on the Zn anode surface after 1 min of the Zn plating, which grows rapidly and finally aggregates into large dendrites due to uneven Zn^{2+} deposition under the ''tip effect''. In comparison, the Zn anode exhibits a uniform and dense Zn plating morphology in BPE, and no Zn dendrite is formed after 30 min, suggesting even nucleation and uniform growth (Fig. 5c). Therefore, the unique nanostructure of BPE can guide uniform Zn^{2+} deposition and contribute to the dendrite-free Zn anode (Fig. 5d). As evidenced by a laser confocal scanning microscope (LCSM), the 3D LCSM image of the Zn anode displays an obvious dendrite-like surface in ZFE but delivers a flat and dendrite-free surface in BPE (Fig. 5e and Fig. S42, ESI†), and the average surface roughness of the Zn anode in ZFE is 10 times higher than that in BPE.

The crystalline structure of the Zn anode is investigated by X-ray diffraction (XRD) patterns and two-dimensional synchrotron grazing-incidence X-ray diffraction (2D-GIXRD) patterns. The intense XRD peaks between 5° and 20° correspond to the by-product, demonstrating the side reaction in ZFE. In contrast, the peak intensity of the by-product is significantly reduced at both room and low temperatures in BPE, indicating that the side reaction is significantly suppressed (Fig. S43, ESI†). Compared with Zn metal, the diffraction peak of the (002) crystal plane at 36.0° becomes weaker in ZFE but stronger in BPE, and the intensity ratio of the (002) crystal plane to the (001) crystal plane is significantly enhanced in BPE, which suggests that BPE can effectively tailor the crystal orientation, and Zn^{2+} prefers to adopt horizontal deposition rather than vertical deposition, thus suppressing the dendrite growth. The GIXD patterns of the Zn anode disclose the strong (100) and (101) texture formation in ZFE, while BPE affords the isotropic and homogeneous Zn anode with significantly weakened (100) and (101) crystal planes but enhanced (002) crystal planes (Fig. 5f). Moreover, the spots of a by-product are observed in ZFE, but no by-product signal is recognized in BPE. XRD and GIXRD patterns reveal that the BPE suppresses the side reaction and manipulates the orientational Zn deposition toward a highly reversible Zn anode.

Full-cell performance

The electrochemical performance of $Zn\|V_2O_5$ full cell assembled with BPE is studied. As demonstrated in Fig. 6a, $Zn\|V_2O_5$ full cell with BPE delivers a high reversible specific capacity of 419.46 mA h g^{-1} after 200 cycles at a current density of 0.5 A g^{-1} with a capacity retention of 100% and CE of 100%. In ZFE, an initial capacity of 397.52 mA h g^{-1} is observed, which gradually decreases to 309.44 mA h g^{-1} after 200 cycles (capacity retention of 70.6%). The capacity of 415.68 mA h g^{-1}, 390.22 mA h g^{-1}, 372.91 mA h g^{-1}, 331.86 mA h g^{-1}, 298.62 mA h g^{-1}, 273.54 mA h g^{-1}, 246.95 mA h g^{-1} and 227.87 mA h g^{-1} can be achieved as the current density increases from 0.5 A g^{-1} to 1 A g^{-1}, 3 A g^{-1}, 5 A g^{-1}, 8 A g^{-1}, 10 A g^{-1}, 12 A g^{-1} and 15 A g^{-1}, respectively (Fig. 6b, c and Fig. S44, ESI†). When the current density goes back to 0.5 A g^{-1}, the discharge capacity returns to 410.65 mA h g^{-1} immediately, indicating the excellent rate performance with BPE compared to ZFE. At a current density of 10 A g^{-1}, a reversible capacity of 249.47 mA h g^{-1} can be achieved after 7000 cycles with a high-capacity retention of 100% in BPE (Fig. 6d), while the capacity in ZFE decreases dramatically to about 42.89 mA h g^{-1} with an inferior capacity retention of only 20.7%. Considering the practical conditions, a limited Zn metal anode (20 μm Zn foil, N/P = 2.55 : 1), a high mass loading of 14 mg cm^{-2}, and a lean BPE (8.7 μL mA^{-1} h^{-1}) are employed for the assembly of full cells. The $Zn\|V_2O_5$ full cell stably operates more than 2000 cycles with a high retention of 84% of its initial capacity at 1 A g^{-1} (Fig. 6e). However, the capacity of the full cell with ZFE rapidly decreases to 30 mA h g^{-1} after activation. More importantly, the long-term cycling performance of the BPE at −60 °C is also investigated. As presented in Fig. 6f, a high specific capacity of 148.5 mA h g^{-1} at 1.0 A g^{-1} with a capacity retention of 100% can be achieved even over 1100 cycles, indicating excellent low-temperature cycle stability. In addition, a high specific capacity of 83 mA h (71.9% of initial capacity) at 25 °C and 57 mA h (78.8% of initial capacity) at −20 °C after 200 cycles can be achieved for the pouch cell (Fig. 6g), and the assembled pouch cell can power a lamp (Fig. 6h), which may endow the BPE with more possibility in practical applications.

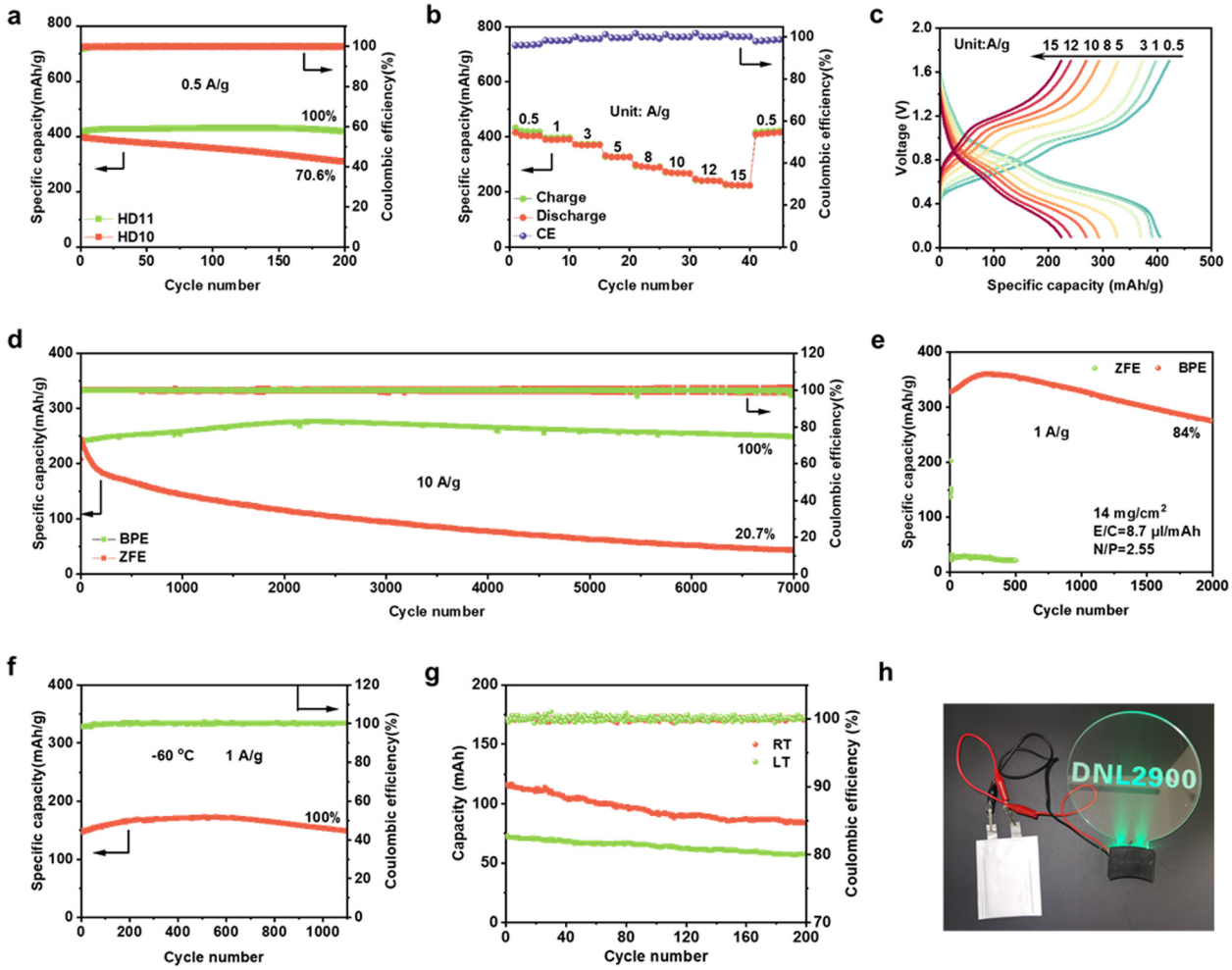

Fig. 6 Electrochemical performances of Zn‖V_2O_5 batteries. (a) Specific capacity profiles at 0.5 A g^{-1}. (b) Rate performances of Zn‖V_2O_5 batteries at different current densities. (c) Discharge–charge curves at different current densities. (d) Long-term cycling performance and corresponding discharge–charge curves of Zn‖V_2O_5 batteries with the ZFE and BPE at 10 A g^{-1}. (e) Long-term cycling performance of Zn‖V_2O_5 batteries with the BPE with a low N/P (2.55), lean electrolyte (8.7 μL mA^{-1} h^{-1}) and high mass loading (14 mg cm^{-2}). (f) Cycling performance of Zn‖V_2O_5 batteries at 1 A g^{-1} under −60 °C. (g) Cycling performance of pouch cell at 0.5 A g^{-1} under room and low temperatures. (h) Photo image of the pouch cell powered lamp.

Conclusions

In this contribution, BPE with both continuous aqueous phase and continuous organic solvent phase is developed for aqueous ZIBs working at ultralow temperature by the systematic investigation of electrolyte nanostructure and elaborate section of volume ratio of H_2O/organic solvent. BPE delivers the optimal Zn^{2+} transfer number of 0.68 and fast desolvation kinetics due to the bicontinuous-phase nanostructure and exhibits a low freezing point below −100 °C and an expanded voltage window due to HB network reconstruction. More importantly, BPE possesses a well-balanced organic solvent-rich solvation sheath and anion-involved solvation sheath and also generates a uniform *in situ* solid electrolyte interface with an organic-rich outer layer and an inorganic-rich inner layer, which inhibits HER and guides uniform Zn^{2+} deposition to achieve highly reversible Zn anode at both room and low temperatures. Consequently, Zn anodes with BPE can stably perform up to 13 000 hours at 25 °C, over 640 hours at a high DOD of 85.4%, and 1400 hours under −60 °C. Zn‖V_2O_5 full cell with the BPE is performed for more than 2000 cycles with a high retention of 84% at the limited Zn metal anode (N/P = 2.55 : 1), high mass loading of 14 mg cm^{-2} and lean electrolyte (8.7 μL mA^{-1} h^{-1}) and works well for 1100 cycles with a capacity retention of 100% at an ultralow temperature of −60 °C. The in-depth understanding of electrolyte nanostructures builds the bridge between the micro intermolecular force of electrolytes and macro battery performance and offers a novel perspective for designing advanced nanostructured electrolytes for low-temperature batteries.

Author contributions

M. X. and H. D. conceived the idea, designed the experiments, wrote and revised the manuscript. M. X., B. Z., Y. S. and H. D. performed the related measurements and formal analysis. R. G. and Q. M. did and helped the analysis of the XAFS and 2D-GIXD. H. D. and D. L. supervised the project. H. D. and Z. C.

provided the funding acquisition. And all the authors commented on the manuscript.

Data availability

The data supporting this article have been included as part of the ESI.†

Conflicts of interest

There are no conflicts to declare.

Acknowledgements

This work is supported by the Energy Revolution S&T Program of Yulin Innovation Institute of Clean Energy, Grant No. YIICE E411060316. Thanks for the support of the Strategic Priority Research Program of the Chinese Academy of Sciences (China, Grant No. XDB0600000, XDB0600200) and the Postdoctoral Fellowship Program of CPSF (GZB20230726). The authors are grateful for the technical support for Vacuum Interconnected Nanotech Workstation (Nano-X) from Suzhou Institute of Nano-Tech and Nano-Bionics. And the authors would like to thank Dr Rong Huang for the help in TOF-SIMS collection and Dr Qing Zhang for conducting the WAXS characterizations.

References

1 C. S. Rustomji, Y. Yang, T. K. Kim, J. Mac, Y. J. Kim, E. Caldwell, H. Chung and Y. S. Meng, *Science*, 2017, **356**, eaal4263.
2 J. Holoubek, H. Liu, Z. Wu, Y. Yin, X. Xing, G. Cai, S. Yu, H. Zhou, T. A. Pascal, Z. Chen and P. Liu, *Nat. Energy*, 2021, **6**, 303–313.
3 T. Yang, Y. Zheng, Y. Liu, D. Luo, A. Yu and Z. Chen, *Renewables*, 2023, **1**, 2–20.
4 M. Xu, H. Dou, Z. Zhang, Y. Zheng, B. Ren, Q. Ma, G. Wen, D. Luo, A. Yu, L. Zhang, X. Wang and Z. Chen, *Angew. Chem., Int. Ed.*, 2022, **134**, e202117703.
5 H. Dou, M. Xu, Y. Zheng, Z. Li, G. Wen, Z. Zhang, L. Yang, Q. Ma, A. Yu, D. Luo, X. Wang and Z. Chen, *Adv. Mater.*, 2022, **34**, 2110585.
6 T. Sun, S. Zheng, H. Du and Z. Tao, *Nano-Micro Lett.*, 2021, **13**, 204.
7 S. Gao, B. Li, H. Tan, F. Xia, O. Dahunsi, W. Xu, Y. Liu, R. Wang and Y. Cheng, *Adv. Mater.*, 2022, **34**, 2201510.
8 C.-X. Zhao, J.-N. Liu, N. Yao, X. Zeng, A. Chen, P. Dong, Y. Zhang, X. Ma, C. Tang, B.-Q. Li and Q. Zhang, *Renewables*, 2023, **1**, 73–80.
9 N. Zhang, T. Deng, S. Zhang, C. Wang, L. Chen, C. Wang and X. Fan, *Adv. Mater.*, 2022, **34**, 2107899.
10 Y. Zhao, Z. Chen, F. Mo, D. Wang, Y. Guo, Z. Liu, X. Li, Q. Li, G. Liang and C. Zhi, *Adv. Sci.*, 2021, **8**, 2002590.
11 M. Chen, Y. Zhang, G. Xing, S.-L. Chou and Y. Tang, *Energy Environ. Sci.*, 2021, **14**, 3323–3351.
12 N. Zhang, X. Chen, M. Yu, Z. Niu, F. Cheng and J. Chen, *Chem. Soc. Rev.*, 2020, **49**, 4203–4219.
13 Y. Yang, C. Liu, Z. Lv, H. Yang, Y. Zhang, M. Ye, L. Chen, J. Zhao and C. C. Li, *Adv. Mater.*, 2021, **33**, 2007388.
14 G. Liang, J. Zhu, B. Yan, Q. Li, A. Chen, Z. Chen, X. Wang, B. Xiong, J. Fan and J. Xu, *Energy Environ. Sci.*, 2022, **15**, 1086–1096.
15 H. Yu, Y. Zeng, N. W. Li, D. Luan, L. Yu and X. W. Lou, *Sci. Adv.*, 2022, **8**, eabm5766.
16 S.-B. Wang, Q. Ran, R.-Q. Yao, H. Shi, Z. Wen, M. Zhao, X.-Y. Lang and Q. Jiang, *Nat. Commun.*, 2020, **11**, 1–9.
17 N. Wang, X. Dong, B. Wang, Z. Guo, Z. Wang, R. Wang, X. Qiu and Y. Wang, *Angew. Chem., Int. Ed.*, 2020, **59**, 14577–14583.
18 L. Ma, J. Z. Lee, T. P. Pollard, M. A. Schroeder, M. A. Limpert, B. Craven, S. Fess, C. S. Rustomji, C. Wang, O. Borodin and K. Xu, *ACS Energy Lett.*, 2021, **6**, 4426–4430.
19 W. Zhang, Q. Zhao, Y. Hou, Z. Shen, L. Fan, S. Zhou, Y. Lu and L. A. Archer, *Sci. Adv.*, 2021, **7**, eabl3752.
20 S.-J. Zhang, J. Hao, D. Luo, P.-F. Zhang, B. Zhang, K. Davey, Z. Lin and S.-Z. Qiao, *Adv. Energy Mater.*, 2021, **11**, 2102010.
21 P. Wang, S. Liang, C. Chen, X. Xie, J. Chen, Z. Liu, Y. Tang, B. Lu and J. Zhou, *Adv. Mater.*, 2022, **34**, 2202733.
22 W. Chen, S. Guo, L. Qin, L. Li, X. Cao, J. Zhou, Z. Luo, G. Fang and S. Liang, *Adv. Funct. Mater.*, 2022, **32**, 2112609.
23 F. Huang, X. Li, Y. Zhang, Y. Jie, X. Mu, C. Yang, W. Li, Y. Chen, Y. Liu, S. Wang, B. Ge, R. Cao, X. Ren, P. Yan, Q. Li, D. Xu and S. Jiao, *Adv. Mater.*, 2022, **34**, 2203710.
24 V. Verma, R. M. Chan, L. Jia Yang, S. Kumar, S. Sattayaporn, R. Chua, Y. Cai, P. Kidkhunthod, W. Manalastas and M. Srinivasan, *Chem. Mater.*, 2021, **33**, 1330–1340.
25 A. Naveed, H. Yang, J. Yang, Y. Nuli and J. Wang, *Angew. Chem., Int. Ed.*, 2019, **58**, 2760–2764.
26 X. Wu, Y. Xu, C. Zhang, D. P. Leonard, A. Markir, J. Lu and X. Ji, *J. Am. Chem. Soc.*, 2019, **141**, 6338–6344.
27 F. Wang, O. Borodin, T. Gao, X. Fan, W. Sun, F. Han, A. Faraone, J. A. Dura, K. Xu and C. Wang, *Nat. Mater.*, 2018, **17**, 543–549.
28 M. Yang, J. Zhu, S. Bi, R. Wang and Z. Niu, *Adv. Mater.*, 2022, **34**, 2201744.
29 Q. Ni, H. Jiang, S. Sandstrom, Y. Bai, H. Ren, X. Wu, Q. Guo, D. Yu, C. Wu and X. Ji, *Adv. Funct. Mater.*, 2020, **30**, 2003511.
30 L. Geng, J. Meng, X. Wang, C. Han, K. Han, Z. Xiao, M. Huang, P. Xu, L. Zhang, L. Zhou and L. Mai, *Angew. Chem., Int. Ed.*, 2022, **61**, e202206717.
31 X. Lin, G. Zhou, M. J. Robson, J. Yu, S. C. T. Kwok and F. Ciucci, *Adv. Funct. Mater.*, 2022, **32**, 2109322.
32 Q. Zhang, K. Xia, Y. Ma, Y. Lu, L. Li, J. Liang, S. Chou and J. Chen, *ACS Energy Lett.*, 2021, **6**, 2704–2712.
33 P. Sun, L. Ma, W. Zhou, M. Qiu, Z. Wang, D. Chao and W. Mai, *Angew. Chem., Int. Ed.*, 2021, **60**, 18247–18255.
34 K. Zhao, G. Fan, J. Liu, F. Liu, J. Li, X. Zhou, Y. Ni, M. Yu, Y.-M. Zhang, H. Su, Q. Liu and F. Cheng, *J. Am. Chem. Soc.*, 2022, **144**, 11129–11137.

35 L. Miao, R. Wang, S. Di, Z. Qian, L. Zhang, W. Xin, M. Liu, Z. Zhu, S. Chu, Y. Du and N. Zhang, *ACS Nano*, 2022, **16**, 9667–9678.
36 Q. Zhang, Y. Ma, Y. Lu, L. Li, F. Wan, K. Zhang and J. Chen, *Nat. Commun.*, 2020, **11**, 4463.
37 Z. Hou, H. Tan, Y. Gao, M. Li, Z. Lu and B. Zhang, *J. Mater. Chem. A*, 2020, **8**, 19367–19374.
38 R. Qin, Y. Wang, M. Zhang, Y. Wang, S. Ding, A. Song, H. Yi, L. Yang, Y. Song and Y. Cui, *Nano Energy*, 2021, **80**, 105478.
39 Y. Zhang, M. Zhu, K. Wu, F. Yu, G. Wang, G. Xu, M. Wu, H.-K. Liu, S.-X. Dou and C. Wu, *J. Mater. Chem. A*, 2021, **9**, 4253–4261.
40 J. Cui, X. Liu, Y. Xie, K. Wu, Y. Wang, Y. Liu, J. Zhang, J. Yi and Y. Xia, *Mater. Today Energy*, 2020, **18**, 100563.
41 L. Miao, R. Wang, W. Xin, L. Zhang, Y. Geng, H. Peng, Z. Yan, D. Jiang, Z. Qian and Z. Zhu, *Energy Storage Mater.*, 2022, **49**, 445–453.
42 N. Chang, T. Li, R. Li, S. Wang, Y. Yin, H. Zhang and X. Li, *Energy Environ. Sci.*, 2020, **13**, 3527–3535.
43 W. Zhao, Z. Pan, Y. Zhang, Y. Liu, H. Dou, Y. Shi, Z. Zuo, B. Zhang, J. Chen and X. Zhao, *Angew. Chem., Int. Ed.*, 2022, **60**, e202205187.
44 X. Zhao, X. Zhang, N. Dong, M. Yan, F. Zhang, K. Mochizuki and H. Pan, *Small*, 2022, **18**, 2200742.
45 Y. Ma, Q. Zhang, L. Liu, Y. Li, H. Li, Z. Yan and J. Chen, *Natl. Sci. Rev.*, 2022, **9**, nwac051.
46 H. Du, K. Wang, T. Sun, J. Shi, X. Zhou, W. Cai and Z. Tao, *Chem. Eng. J.*, 2022, **427**, 131705.
47 H. Lu, J. Hu, L. Wang, J. Li, X. Ma, Z. Zhu, H. Li, Y. Zhao, Y. Li, J. Zhao and B. Xu, *Adv. Funct. Mater.*, 2022, **32**, 2112540.
48 Q. Nian, J. Wang, S. Liu, T. Sun, S. Zheng, Y. Zhang, Z. Tao and J. Chen, *Angew. Chem., Int. Ed.*, 2019, **58**, 16994–16999.
49 D. Feng, F. Cao, L. Hou, T. Li, Y. Jiao and P. Wu, *Small*, 2021, **17**, 2103195.
50 L. Cao, D. Li, E. Hu, J. Xu, T. Deng, L. Ma, Y. Wang, X.-Q. Yang and C. Wang, *J. Am. Chem. Soc.*, 2020, **142**, 21404–21409.
51 S. Liu, J. Mao, W. K. Pang, J. Vongsvivut, X. Zeng, L. Thomsen, Y. Wang, J. Liu, D. Li and Z. Guo, *Adv. Funct. Mater.*, 2021, **31**, 2104281.
52 G. Ma, L. Miao, W. Yuan, K. Qiu, M. Liu, X. Nie, Y. Dong, N. Zhang and F. Cheng, *Chem. Sci.*, 2022, **13**, 11320–11329.
53 F. Ming, Y. Zhu, G. Huang, A.-H. Emwas, H. Liang, Y. Cui and H. N. Alshareef, *J. Am. Chem. Soc.*, 2022, **144**, 7160–7170.
54 B. Kakoty, R. Vengarathody, S. Mukherji, V. Ahuja, A. Joseph, C. Narayana, S. Balasubramanian and P. Senguttuvan, *J. Mater. Chem. A*, 2022, **10**, 12597–12607.
55 D. S. Liu, Y. Zhang, S. Liu, L. Wei, S. You, D. Chen, M. Ye, Y. Yang, X. Rui and Y. Qin, *Adv. Funct. Mater.*, 2022, **32**, 2111714.
56 X. Lu, L. Tao, K. Qu, A. Amardeep and J. Liu, *Adv. Funct. Mater.*, 2023, **33**, 2211736.
57 X. Song, H. He, M. H. A. Shiraz, H. Zhu, A. Khosrozadeh and J. Liu, *Chem. Commun.*, 2021, **57**, 1246–1249.
58 Z. Hou, Z. Lu, Q. Chen and B. Zhang, *Energy Storage Mater.*, 2021, **42**, 517–525.
59 T. C. Li, Y. Lim, X. L. Li, S. Luo, C. Lin, D. Fang, S. Xia, Y. Wang and H. Y. Yang, *Adv. Energy Mater.*, 2022, **12**, 2270060.
60 Y. Shang, P. Kumar, T. Musso, U. Mittal, Q. Du, X. Liang and D. Kundu, *Adv. Funct. Mater.*, 2022, **32**, 2200606.
61 D. Wang, D. Lv, H. Liu, S. Zhang, C. Wang, C. Wang, J. Yang and Y. Qian, *Angew. Chem., Int. Ed.*, 2022, **61**, e202212839.
62 S. Liu, J. Vongsvivut, Y. Wang, R. Zhang, F. Yang, S. Zhang, K. Davey, J. Mao and Z. Guo, *Angew. Chem., Int. Ed.*, 2023, **62**, e202215600.
63 Q. Jian, T. Wang, J. Sun, M. Wu and T. Zhao, *Energy Storage Mater.*, 2022, **53**, 559–568.
64 Y. Sun, Z. Xu, X. Xu, Y. Nie, J. Tu, A. Zhou, J. Zhang, L. Qiu, F. Chen and J. Xie, *Energy Storage Mater.*, 2022, **48**, 192–204.
65 F. Wu, Y. Chen, Y. Chen, R. Yin, Y. Feng, D. Zheng, X. Xu, W. Shi, W. Liu and X. Cao, *Small*, 2022, **18**, 2202363.
66 M. Zhang, H. Hua, P. Dai, Z. He, L. Han, P. Tang, J. Yang, P. Lin, Y. Zhang and D. Zhan, *Adv. Mater.*, 2023, **35**, 2208630.
67 S. J. Zhang, J. Hao, Y. Zhu, H. Li, Z. Lin and S. Z. Qiao, *Angew. Chem., Int. Ed.*, 2023, **62**, e202301570.
68 Y. Lyu, J. A. Yuwono, P. Wang, Y. Wang, F. Yang, S. Liu, S. Zhang, B. Wang, K. Davey and J. Mao, *Angew. Chem., Int. Ed.*, 2023, **135**, e202303011.
69 Y. Wang, B. Liang, J. Zhu, G. Li, Q. Li, R. Ye, J. Fan and C. Zhi, *Angew. Chem., Int. Ed.*, 2023, **62**, e202302583.
70 W. Zhang, Y. Dai, R. Chen, Z. Xu, J. Li, W. Zong, H. Li, Z. Li, Z. Zhang and J. Zhu, *Angew. Chem., Int. Ed.*, 2023, **62**, e202212695.
71 Y. Zhang, S. Shen, K. Xi, P. Li, Z. Kang, J. Zhao, D. Yin, Y. Su, H. Zhao and G. He, *Angew. Chem., Int. Ed.*, 2024, **32**, e202407067.
72 C. You, R. Wu, X. Yuan, L. Liu, J. Ye, L. Fu, P. Han and Y. Wu, *Energy Environ. Sci.*, 2023, **16**, 5096–5107.

